Climate change made record breaking early season heat in Argentina and Paraguay about 60 times more likely

Juan Antonio Rivera[1], Paola A. Arias[2] , Anna A. Sörensson[3,4,5], Mariam Zachariah[6], Clair Barnes[6], Sjoukje Philip[7], Sarah Kew[7], Robert Vautard[8], Gerbrand Koren[9], Izidine Pinto[7], Maja Vahlberg[10], Roop Singh[10], Emmanuel Raju[13], Sihan Li[14], Wenchang Yang[15], Gabriel A. Vecchi[15,16], Luke J. Harrington[17] and Friederike E.L. Otto[6]

1. Instituto Argentino de Nivología, Glaciología y Ciencias Ambientales (IANIGLA), CCT CONICET Mendoza, Argentina.
2. Grupo de Ingeniería y Gestión Ambiental (GIGA), Escuela Ambiental, Facultad de Ingeniería, Universidad de Antioquia, Colombia
3. Facultad de Ciencias Exactas y Naturales, Universidad de Buenos Aires, Buenos Aires
4. Centro de Investigaciones del Mar y la Atmósfera,CONICET–Universidad de Buenos Aires, Buenos Aires, Argentina
5. CNRS–IRD–CONICET–UBA, Instituto Franco-Argentino para el Estudio del Clima y sus Impactos (IRL 3351 IFAECI), Buenos Aires, Argentina
6. Grantham Institute, Imperial College London, UK
7. Royal Netherlands Meteorological Institute (KNMI), De Bilt, The Netherlands
8. Institut Pierre-Simon Laplace, Paris, France
9. Copernicus Institute of Sustainable Development, Utrecht University, Utrecht, the Netherlands
10. Red Cross Red Crescent Climate Centre, The Hague, the Netherlands
11. Faculty of Geo-Information Science and Earth Observation (ITC), University of Twente, Enschede, the Netherlands
12. Global Disaster Preparedness Center, American Red Cross, Washington DC, USA
13. Department of Public Health, Global Health Section & Copenhagen Centre for Disaster Research
14. Department of Geography, University of Sheffield
15. Department of Geosciences, Princeton University, Princeton, NJ 08544, USA
16. High Meadows Environmental Institute, Princeton University, Princeton, NJ 08544, USA
17. Te Aka Mātuatua School of Science, University of Waikato, Hillcrest, Hamilton 3214, New Zealand

1 Introduction

Starting mid November 2022, large regions in Northern Argentina and neighboring countries experienced anomalously high temperatures. An area comprising the central-north part of Argentina, southern Bolivia, central Chile, and most of Paraguay and Uruguay, experienced record-breaking temperatures as a consequence of two consecutive heatwaves. From 23 to 29 of November, a heatwave (at least three consecutive days with maximum (TXx) and minimum temperatures (TXn) above the 90th percentile) was declared by the National Weather Service (SMN) of Argentina for 19 stations located in the latitudinal band from 28° to 37°S (SMN, 2022). During this period, temperature anomalies exceeded 5°C over this region and some stations recorded maximum temperatures of more than 40°C. Over Uruguay most stations recorded temperatures above the upper tercile during the last part of November (Inumet, 2022).

A larger area, extending far south towards Patagonia, showed record-breaking temperatures for November, with 14 locations setting new maximum temperature records. In South-Western South America, the Meteorological Office of Chile also reported the occurrence of three consecutive heatwaves over this period, a factor that made this month the warmest November on record (58 years) over Central Chile (BiobioChile, 2022). It is noteworthy that these record temperatures occurred before the beginning of the austral summer season, making them particularly exceptional. Moreover, these events happened just a few days after record-breaking cold conditions took place over central Argentina and Uruguay.

Furthermore, South-Eastern South America has been experiencing a prolonged drought that has affected national agriculture as well as exports. This large-scale drought started in 2019 due to precipitation deficits and has worsened over time (Naumann et al., 2021), likely partly due to the continuing La Niña conditions that tend to have a drying effect on the region (Cai et al., 2020). The high temperatures recorded during the heatwave of January 2022 exacerbated these negative impacts on crops (BBC, 2022), while the heatwave of November 2022 has already contributed to increased soy prices in the international market (Agrositio, 2022). In addition, several wildfires were reported over central-northern Argentina by the end of November (La Voz; 2022, Viapais, 2022; Infobae, 2022). Impacts were also reported in Central Chile, which has been experiencing a 14-years-long megadrought and whose effects were exacerbated with the occurrence of the three consecutive heatwaves observed in November 2022 (El Mostrador, 2022).

A second period of prolonged hot weather was recorded during the first quarter of December 2022, just a few days after the November heatwave. The highest severity was observed in the same latitudinal band of the previous event, although the spatial extension covered roughly half of Argentina, with heatwave durations ranging between 3 and 9 days. According to the SMN, 45 stations recorded heatwave conditions between 4 to 12 of December, with maximum temperatures above 40°C in 24 locations, 4 of them exceeding 45°C. For instance, Rivadavia station, located near the border with Bolivia and Paraguay, recorded 46°C of maximum temperature during December 7, making the region one of the hottest in the World during that day. Averaged over the first 10 days of December, temperature anomalies were above 4°C north of 40°S, with some specific locations exceeding 10°C above normal conditions, particularly between 7 to 9 of December. During this period, 9 locations from northern Argentina registered their highest maximum temperature of December since at least 1961. Energy shortcuts occurred in Buenos Aires city, affecting more than half million people due to the high energy demand (Infobae, 2022). This highlights the vulnerability to heatwaves of the electricity distribution system of the metropolitan area of Buenos Aires, which has almost 7 times more probability of failure compared to cold events (Santágata et al., 2017).

A special bulletin for persistent high temperatures was issued by the Directorate of Meteorology and Hydrology of Paraguay on December 7, with the probability of experiencing a heatwave over much of the country (Dirección de Meteorología e Hidrología, 2022). For instance, western Paraguay registered maximum temperatures above 40°C between 6 to 9 of December, equaling the all-time record at Mariscal Estigarribia during December 8. At the same time, the Uruguayan Institute of Meteorology released a heatwave warning, particularly for the western portion of the country (Instituto Uruguayo de Meteorología, 2022). Central and southern Chile also experienced a prolonged warm period during the first days of December. Santiago de Chile recorded one of the longest heatwaves on record, with a duration of 11 days and the warmest day of 2022 during December 11 (TXx = 35.7°C). During this heatwave Central Chile was affected by a series of forestal wildfires, generating a dense cap of smoke over the capital that resulted in a health risk alert on the 16th of

December (BBC, 2022). Chile has observed more heat records the following week, with 41.6°C in San Felipe on the 15th of December and 41.2°C in Llay Llay in Valparaiso on the 16th of December. More heat is forecast.

The current heatwave is following earlier extreme events – including an unusually cold spring – that have affected the region and resulted e.g. in crop losses (Successful Farming, 2022). The affected region is an important agricultural hub, producing large amounts of wheat (News Dakota, 2022). The heatwave-induced crop losses have economic consequences for the region and for consumers beyond the directly affected region. Furthermore, the affected region, which includes Argentina's capital Buenos Aires, is densely populated and many people are thus affected by the intense heat.

While an accounting of excess deaths related to this heatwave is not yet available, past heat waves in Argentina and Paraguay have resulted in significant human mortality including a December 2013 heatwave that increased total daily deaths by 43% in Buenos Aires, Argentina (Chesini et al., 2019; Chesini et al., 2021), and a study attributing heat related deaths to climate change found that in Paraguay total mortality was modeled to have increased by up to 5% since preindustrial times due solely to more heat-related deaths from climate change (Mitchell, 2021). The earlier heatwave of December 2013 - January 2014 that hit Buenos Aires resulted in power outages (Procupez, 2016) with large societal impact, showing the vulnerability of the region.

An important geographical element affecting atmospheric circulation and climate in South-Eastern and South-Western South America are the Andes Mountains, favoring the meridional transport of air masses between the tropics and the South-Eastern midlatitudes (Rusticucci, 2012). South-Western South America is also influenced by the interaction of the strong westerly winds with the extratropical Andes as well as by the Pacific Ocean and the South Pacific Subtropical High (e.g. Espinoza et al. 2020). By contrast, South-Eastern South America is more affected by the South Atlantic Subtropical High (e.g. Sun et al., 2017), the South Atlantic Convergence Zone (SACZ, e.g. Barros et al., 2000) and the interactions with the South American Monsoon System, which control atmospheric circulation patterns in this region.

Typically, heatwaves are linked to a persistent atmospheric blocking that favors the presence of warm air masses for several consecutive days over South-Eastern and South-Western South America. This can contribute to high temperature anomalies which might be reinforced if the regions are affected by drought conditions due to extremely low soil moisture (Alvarez et al., 2019; Marengo et al., 2022). The persistence of an anticyclonic circulation at various levels of the troposphere favors subsidence conditions and intense solar heating, intensifying the warming process, which might also be reinforced by horizontal temperature advection and an intensification of the SACZ (Campetella and Rusticucci, 1998; Cerne et al., 2007; Alvarez et al., 2019).

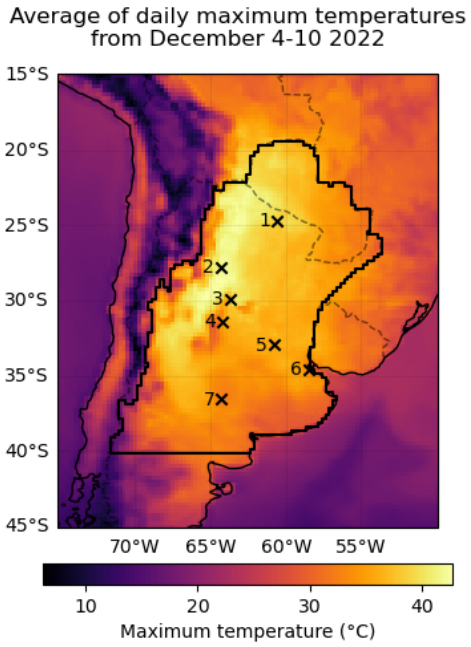

Figure 1: ERA5 near surface temperature (T2m) [℃] showing 7-day average daily maximum for the period of the 4th to 10th of December 2022. The bold black outline represents the study region and the crosses mark stations used in the observational analysis: 1. Las Lomitas; 2. Santiago del Estero; 3. Villa María del Río Seco; 4. Córdoba; 5. Rosario; 6. Buenos Aires; 7. Santa Rosa

To investigate the extent to which human-caused climate change altered the frequency of occurrence of the extremely high temperatures, across the region affected by the most extreme heat (see Fig. 1), we choose to analyse the 2-m temperature over land in the region covering northern Argentina and Paraguay and excluding high altitudes (highlighted by black outline in Fig. 1). This region includes the areas under red alert from the Argentinian Weather Service and includes the cities with the highest impacts. To account for the event itself, which lasted for about a week with durations at different locations ranging from 3-9 days, we decided to analyse the annual (July-June) maximum of the 7-day average of daily maximum temperatures over this region. Fig. 1 shows the 2022 event that occurred during 4-10 December.

Additionally, we analyse the change in frequency and intensity of the maximum observed 7-daily temperature of 2022 at 7 locations, indicated as crosses in Fig 1. These include the cities of Buenos Aires, Córdoba and Rosario.

The Sixth Assessment Report (AR6) of the Intergovernmental Panel on Climate Change (IPCC) assesses that it is virtually certain that the duration, frequency and intensity of hot extreme events at global scale, such as heatwaves, are increasing due to human activity (IPCC 2021; Seneviratne et al. 2021). Over most of the South American continent, an increase in the intensity and frequency of heatwave events between 1961 and 2014 has been detected (Ceccherini et al., 2016; Rusticucci et al., 2016; Geirinhas et al., 2018), with high confidence in the attribution to human activity in South-Eastern South America and medium confidence in South-Western South America (Seneviratne et al. 2021). In Argentina, the mean warming is below the global average warming, however, a marked increase in the occurrence and duration of heatwaves has been observed (Barros et al., 2015; Lovino et al., 2018). The heatwave that affected northern and central Argentina in December 2013

was found to have been exacerbated by anthropogenic forcings, with best-guess estimates of the event probability increasing by a factor of five (Hannart et al., 2015; Otto et al., 2017). A storyline attribution study for the 2011/2012 drought for the South-Eastern South American region highlighted the complex interactions between increased precipitation and increased temperatures for this region (van Garderen and Mindlin, 2022), which is relevant for the present heatwave occurring during the multi-year drought that started in 2019. Globally, compound drought and heatwave events increased significantly in the last 4 decades over wheat-producing areas, making northern Argentina a hotspot region (He et al., 2022).

IPCC 2021 assessed that it is very likely that the intensity and frequency of hot extremes will continue increasing in South America, compared with the 1995–2014 baseline, even under 1.5°C global warming, while such an increase is virtually certain to occur under 4°C global warming (see Table 11.13 of Seneviratne et al. 2021 and Table 12.6 of Ranasinghe et al., 2021). This is also true for Argentina, where the observed trend of heatwaves is expected to increase substantially even for moderate warming scenarios (Rusticucci et al., 2016).

Among the impacts of warming temperatures is the emergence of dengue in temperate latitudes, with increasing populations of *Aedes aegypti* (Robert et al., 2019, 2020; Estallo et al., 2020; López et al., 2021). The IPCC AR6 assesses that the future increases in the number of months favorable for the transmission of dengue will be highest in South-Eastern South America in comparison to other regions in the continent (Castellanos et al. 2022), and extreme hot events such as heatwaves could exacerbate this. For South-Western South America, the number of fires and areas burned by wildfires have increased significantly from 1946 to 2017, especially in Chile, partly due to increases in temperature, threatening biodiversity (González et al., 2011; Jolly et al., 2015; Úbeda and Sarricolea, 2016; de la Barrera et al., 2018; Urrutia-Jalabert et al., 2018). In general, a more frequent occurrence of intense and long heatwaves has negative impacts in water and food systems, human health, terrestrial and freshwater ecosystems, among other systems that exhibit high or very high vulnerability in South-Eastern and South-Western South America (Castellanos et al. 2022).

2 Data and methods

2.1 Observational data

We use the ERA5 reanalysis from the European Centre for Medium-Range Weather Forecasts (Hersbach et al., 2020) for fitting probability distributions to maximum temperatures in the study region and analysing the heatwave event in question in the context of climate change. The reanalysis that runs up to the end of November 2022 is supplemented with analysis data up to 11 December. The recent maximum over 7 days occurred between 4 and 10 December.

The second dataset is the gridded dataset of daily temperature known as the CPC Global Unified Daily Gridded Temperature data, that is provided by the NOAA PSL, Boulder, Colorado, USA, from their website. This data is available at 0.5° x 0.5° resolution, for the period 1979-present and it has been used for analysing the heatwave event. As a measure of anthropogenic climate change we use the (low-pass filtered) global mean surface temperature (GMST), where GMST is taken from the National Aeronautics and Space Administration (NASA) Goddard Institute for Space Science (GISS) surface temperature analysis (GISTEMP; Hansen et al., 2010; Lenssen et al. 2019).

Time series of daily maximum and minimum temperatures from January 1961 to December 12th 2022 at the locations shown in Figure 1 were used to validate the ERA5 reanalysis and to evaluate local trends in return times. These station data were provided by Argentina's National Weather Service. The

selected stations cover the three largest cities in Argentina (Buenos Aires, Córdoba and Rosario), with three sites in the hottest part of the December heatwave, and one (Santa Rosa) in the cooler southern region.

2.2 Model and experiment descriptions

We used several model ensembles with different characteristics (resolution, coupling, processes etc), as follows:

1. **CMIP6**: We used all simulations of the daily maximum temperature available at the Institut Pierre-Simon Laplace (IPSL) Earth System Grid Federation (ESGF) node from their first realization (denoted r1iXpYfZ), where X, Y and Z can vary (but we select only one of each), without considering ensembles, as they have a very heterogeneous number of members. This led to the selection of 28 simulations from different coupled models. The resolution varies depending on the model but stays above 50 km. All temperatures are projected onto a 0.25°x0.25° grid before being spatially averaged over the study region (see figure 1). For more details on CMIP6, please see Eyring et al., (2016).

2. **CORDEX**: We used all CORDEX simulations available at the IPSL ESGF node, separating them into two ensembles: CORDEX SAM-44 (14 different models with 0.44° resolution, i.e. about 50 km; Falco et al., 2018) and CORDEX SAM-22 (6 different models with resolution of 0.22°, about 25 km;). CORDEX simulations result from a dynamical downscaling, using a regional climate model, of a general circulation model. As for CMIP6 simulations, temperatures are projected onto a 0.25°x0.25° grid (Gutowski Jr. et al., 2016) before being spatially averaged over the study region.

3. **HighResMIP**: This is an SST-forced model ensemble (Haarsma et al. 2016), the simulations for which span from 1950 to 2050. The SST and sea ice forcings for the period 1950-2014 are obtained from the 0.25° x 0.25° Hadley Centre Global Sea Ice and Sea Surface Temperature dataset that have undergone area-weighted regridding to match the climate model resolution (see Table B). For the 'future' time period (2015-2050), SST/sea-ice data are derived from RCP8.5 (CMIP5) data, and combined with greenhouse gas forcings from SSP5-8.5 (CMIP6) simulations (see Section 3.3 of Haarsma et al. 2016 for further details).

4. **FLOR and AM2.5C360 models**: The FLOR (Vecchi et al. 2014) and AM2.5C360 (Yang et al. 2021, Chan et al. 2021) climate models are developed at Geophysical Fluid Dynamics Laboratory (GFDL). The FLOR model is an atmosphere-ocean coupled GCM with a resolution of 50 km for land and atmosphere and 1 degree for ocean and ice. Ten ensemble simulations from FLOR are analysed, which cover the period from 1860 to 2100 and include both the historical and RCP4.5 experiments driven by transient radiative forcings from CMIP5 (Taylor et al. 2012). The AM2.5C360 is an atmospheric GCM based on that in the FLOR model (Delworth et al. 2012, Vecchi et al. 2014) with a horizontal resolution of 25 km. Three ensemble simulations of the Atmospheric Model Intercomparison Project (AMIP) experiment (1871-2050) are analysed. These simulations are initialised from three different pre-industrial conditions but forced by the same SSTs from HadISST1 (Rayner et al. 2003) after groupwise adjustments (Chan et al. 2021) over 1871-2020. SSTs between 2021 and 2050

are using the FLOR RCP4.5 experiment 10-ensemble mean values after bias correction. Radiative forcings are using historical values over 1871-2014 and RCP4.5 values after that.

5. **UKCP18 land-GCM:** This is a fifteen-member perturbed physics ensemble developed by the UK Met Office (Murphy et al., 2018). The ensemble members are derived from HadGEM3-GC3.05, a high-resolution coupled ocean-atmosphere model with horizontal grid spacing of approximately 60km at mid-latitudes, which includes an explicit representation of atmospheric aerosols.

2.3 Statistical methods

In this analysis we analyse time series from the region in the north of Argentina and Paraguay for July-June annual maxima of daily maximum temperature values (TX7x) where long records of observed data are available. Methods for observational and model analysis and for model evaluation and synthesis are used according to the World Weather Attribution Protocol, described in Philip et al. (2020), with supporting details found in van Oldenborgh et al. (2021), Ciavarella et al. (2021) and here.

The analysis steps include: (i) trend calculation from observations; (ii) model validation; (iii) multi-method multi-model attribution and (iv) synthesis of the attribution statement.
We calculate the return periods, Probability Ratio (PR; the factor-change in the event's probability) and change in intensity of the event under study in order to compare the climate of now and the climate of the past, defined respectively by the GMST values of now and of the preindustrial past (1850-1900, based on the Global Warming Index https://www.globalwarmingindex.org). To statistically model the event under study, we use a GEV that shifts with GMST. Next, results from observations and models that pass the validation tests are synthesized into a single attribution statement.

3 Observational analysis: return period and trend

3.1 Analysis of point station data

Fig. 2 shows the time series of the annual maxima of 7-day average daily maxima for the seven selected stations (Fig. 1) - Las Lomitas, Santiago del Estero, Villa María del Río Seco, Córdoba, Rosario, Buenos Aires and Santa Rosa. We use this data for validating the performance of the gridded reanalyses products that are considered for this study. To do this, the station-based time series are overlaid with the values for the corresponding closest cell in ERA5 reanalysis dataset, and the ERA5 regional mean. The station observations and the reanalysis-based values are found to be in good agreement for all stations (correlation > 0.7; statistically significant), lending confidence to the choice of ERA5 for capturing the event.

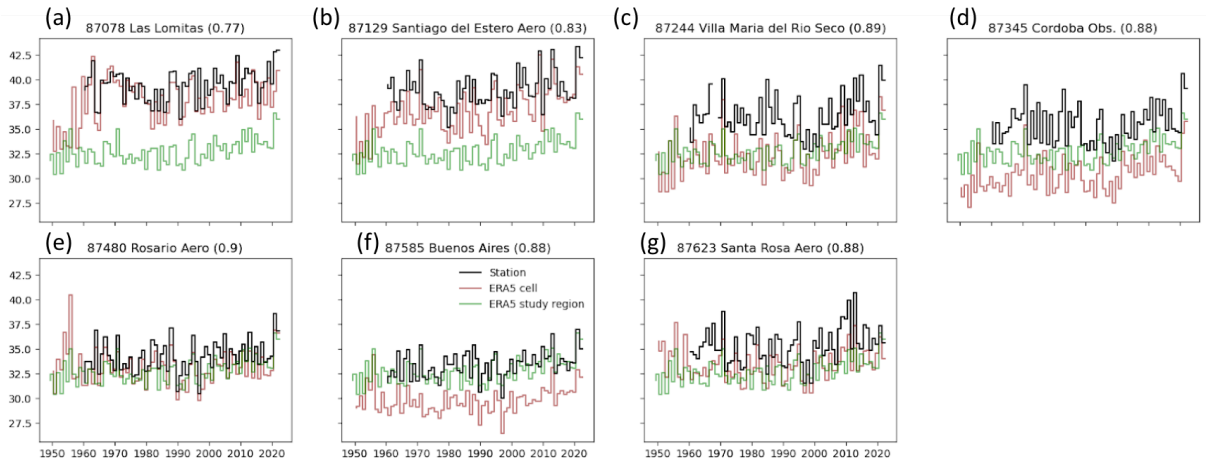

Figure 2: 7-day annual (July-June) maximum temperature at (a) Las Lomitas, (b) Santiago del Estero, (c) Villa María del Río Seco, (d) Córdoba, (e) Rosario, (f) Buenos Aires and (g) Santa Rosa, for the period 1961-2022. The red and the green lines show the corresponding estimates from the closest cell and the average over the study region, from ERA5 reanalysis dataset, available for the years 1950-2022.

For each of these stations that are situated inside the study region, we also estimate the return period, the probability ratios and the intensity changes, as shown in Table 1. The 7-day maximum temperatures as high as those observed this year have return times ranging from 4 to 40 years, but the heat is rarer towards the northwest of the region. The 2022 event in Las Lomitas (Station 1 in Fig. 1) that incidentally records the highest temperature among these stations, would have been unlikely in a world without climate change (PR>100).

Table 1: 7-day maximum temperature in the year 2022, and the best estimates for return period, probability ratio and intensity change at seven individual stations in the study region.

Station		**Event magnitude [°C]**	**Return period**	**Probability ratio (PR)**	**Intensity change (I)**
No.	**Name**				
1	Las Lomitas	43.014	40.4380	1000000	1.804
2	Santiago del Estero	42.257	15.1540	3.8982	1.385
3	Villa Maríia del Ríio Seco	39.986	15.6070	1.6568	0.686
4	Cóordoba	39.100	17.2010	2.3102	0.984
5	Rosario	36.814	8.7029	7.4739	1.566
6	Buenos Aires	34.986	3.9540	9.5516	1.695
7	Santa Rosa	35.629	1.6589	2.3926	1.742

3.2 Analysis of gridded data

Fig. 3(a) shows the time-series of annual 7-day maximum of daily maximum temperature for the study region based on the two observed datasets- ERA5 (Fig. 3(a)) and CPC (Fig. 3(b)). There is an increasing trend in this variable in both datasets, in particular for the period 1979-2022 that is common to both datasets.

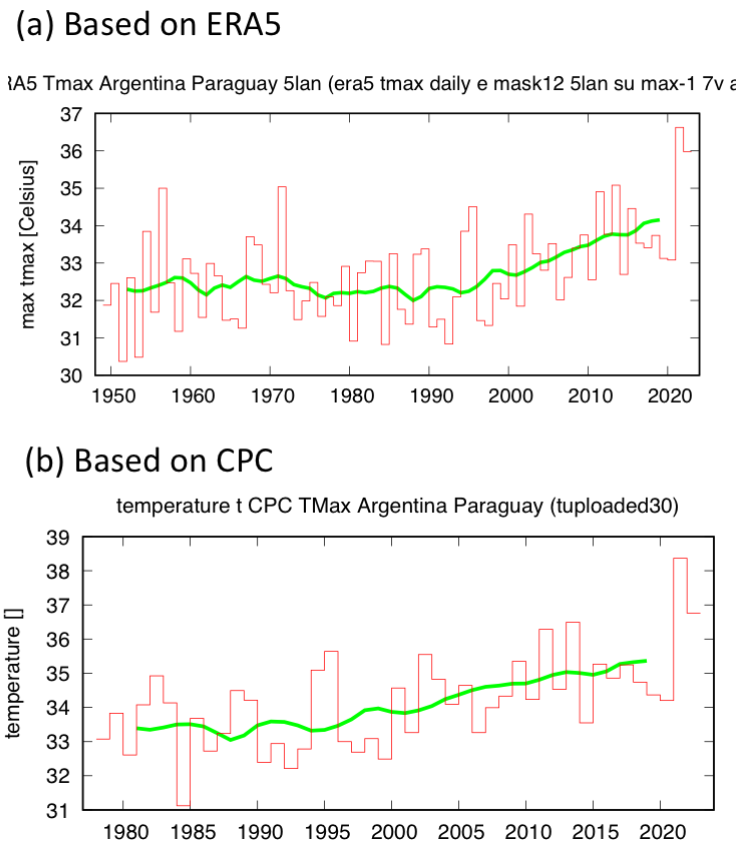

Figure 3: Time series of annual 7-day maximum temperature, area-averaged over the study domain along with the 10 year running mean (shown by green line) based on (a) ERA5 and (b) CPC datasets.

The left panels in Fig. 4 show the response of the study area-averaged annual 7-day maximum temperature based on ERA5 (Fig. 4(a *left*)) and CPC (Fig. 4(b *left*)) to observed GMST anomalies. The right panels (Fig. 4(a-b)) show the return period curves for the current, 2022 climate and a past climate that would have been 1.2degC cooler as compared to now, based on the respective datasets. Based on ERA5, the return period of the 2022 event in the current climate is 1-in-20 years, whereas the event is found to occur more frequently now in the CPC dataset, with a return period of 10 years. The probability ratios suggest the tendency of such events becoming hotter and more frequent due to climate change. The probability ratio is 26 (6-inf) based on ERA5 and 280 (13-inf) from CPC data, with intensity changes of 2.15degC (1.3-3) and 3.75degC (2.2-5.3), respectively.

Although there is a general agreement between the two datasets in their annual variability (Fig. 2) and their fits (Table 2), the CPC dataset is shorter (beginning in the year 1979), as opposed to ERA5 beginning in 1950. A careful examination of the trends in Fig. 4 also reveal a higher trend since 1980 in the ERA5 data that may have partially influenced this difference in the return periods, probability ratios and intensity changes. Therefore, we select the longer ERA5 as the primary dataset for the event

definition and for model evaluation. The return period used for model analysis for the annual 7-day maximum temperature is 20 years.

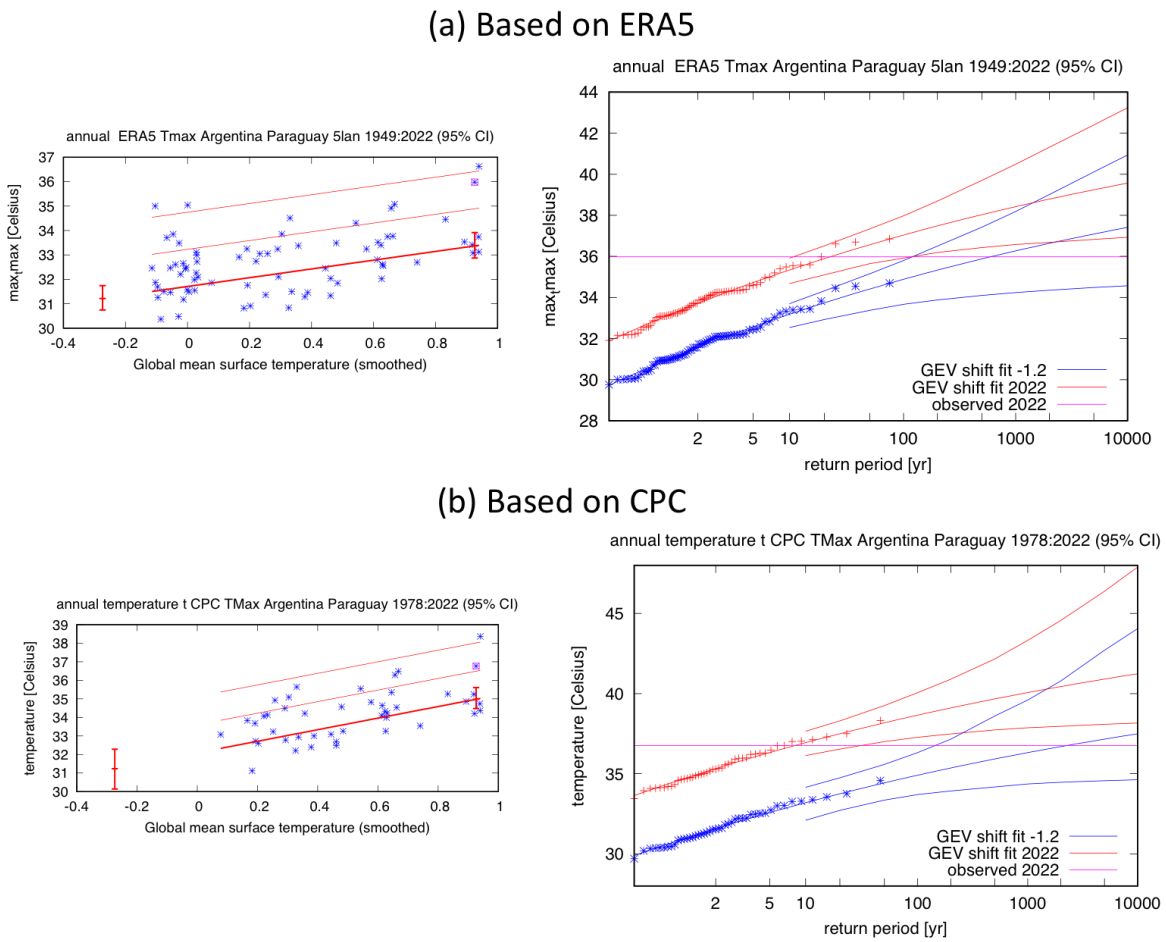

Figure 4: (a) Response of annual maxima of 7-day maximum temperature, averaged over the study region to change in global mean temperature, based on ERA5 dataset. The thick red line denotes the time-varying mean, and the thin red lines show 1 standard deviation (s.d) and 2 s.d above. The vertical red lines show the 95% confidence interval for the location parameter, for the current, 2022 climate and the hypothetical, 1.2ºC cooler climate. The 2022 observation is highlighted with the magenta box. (b) GEV-based return periods for the 2022 climate (red lines) and the 1.2ºC cooler climate (blue lines with 95% CI), based on ERA5 dataset. (c) same as (a), based on CPC dataset. (d) same as (b), based on CPC dataset.

4 Model evaluation

In the subsections below we show the results of the model validation for the study region (Table 2) . Per framing or model setup, we use models that only just pass the validation tests, if we only have five models or less for that framing that performs well. The climate models are evaluated against the observations in their ability to capture:

1. Seasonal cycles: For this, we qualitatively compare the model outputs against observations-based plots. We discard the models that exhibit multi-modality and/or ill-defined peaks in their seasonal cycles. We also discard the model if the rainy season onset/termination varies significantly from the observations.

2. Spatial patterns: Models that do not match the observations in terms of the large-scale precipitation patterns are excluded.

3. Parameters of the fitted GEV model. We discard the model if the model and observation parameters ranges do not overlap.

The models are labelled as 'good','reasonable', or 'bad' based on their performances in terms of the three criteria discussed above. Finally, if the model is 'good' for all of these criteria, we give it an overall rating of 'good' (green highlight in Table 2). We rate the model as 'reasonable' or 'bad', if it is rated 'reasonable' or 'bad', respectively, for at least one of the three criteria. These are respectively shown by the yellow and red highlights in Table 2.

Table 2. Evaluation results of the climate models considered for attribution analysis of the annual 7-day maximum temperature over the study domain. The table consists of qualitative assessments of the seasonal cycles and spatial patterns, and the sigma and shape parameters from fitting a GEV distribution that shifts with GMST and the magnitude of the 1-in- 20 year event in the 2022 climate.

Observations	**Seasonal cycle**	**Spatial pattern**	**Sigma**	**Shape**	**Event magnitude [°C]**
ERA5			0.957 (0.813 ... 1.09)	-0.082 (-0.23 ... 0.038)	38.9892
CPC			0.949 (0.701 ... 1.12)	-0.077 (-0.29 ... 0.12)	40.56
Model					**Threshold for 20-yr return period**
FLOR historical-rcp4.5 (10)	good	good	1.53 (1.43 ... 1.62)	-0.25 (-0.29 ... -0.21)	37.973
AM2.5C360 amipHistorical+rcp4.5SST (3)	good	good	1.43 (1.26 ... 1.57)	-0.20 (-0.29 ... 0.12)	39.516
CORDEX44-CANESMr1-RCA ()	good	good	0.770 (0.600 ... 0.920)	-0.31 (-0.62 ... -0.070)	
CORDEX44-CANESMr1-WRF341 ()	good	good	0.720 (0.570 ... 0.880)	-0.13 (-0.49 ... 0.050)	
CORDEX44-CNRMr1-RCA ()	good	good	0.850 (0.620 ... 1.02)	-0.22 (-0.39 ... 0.030)	
CORDEX44-MK3r1-RCA ()	good	good	0.910 (0.690 ... 1.11)	-0.14 (-0.43 ... 0.10)	
CORDEX44-ECEARTHr12-RCA ()	good	good	0.770 (0.620 ... 0.910)	-0.17 (-0.35 ... 0.020)	
CORDEX44-IPSLr1-RCA ()	good	good	0.870 (0.630 ... 1.03)	-0.23 (-0.38 ... -0.050)	
CORDEX44-CORDEX44-MIROCr1-RCA ()	good	good	0.850 (0.710 ... 0.990)	-0.18 (-0.40 ... 0.040)	
CORDEX44-HADGEMr1-REGCM ()	good	good	0.690 (0.520 ... 0.840)	0.10 (-0.12 ... 0.36)	
CORDEX44-HADGEMr1-RCA ()	good	good	1.08 (0.830 ... 1.29)	-0.36 (-0.56 ... -0.17)	
CORDEX44-MPIr1-REMO ()	good	good	0.970 (0.750 ... 1.16)	-0.15 (-0.37 ... 0.080)	
CORDEX44-MPIr1-RCA ()	good	good	0.840 (0.680 ... 0.970)	-0.10 (-0.27 ... 0.050)	
CORDEX44-NORESMr1-RCA ()	good	good	0.840 (0.670 ... 1.00)	-0.15 (-0.46 ... 0.030)	
CORDEX44-GFDLr1-REGCM ()	good	good	1.06 (0.860 ... 1.26)	-0.28 (-0.57 ... -0.090)	
CORDEX44-GFDLr1-RCA ()	good	good	0.940 (0.740 ... 1.10)	-0.33 (-0.59 ... -0.16)	
HighResMIP-CNRM-CM6-1 (1)	good	good	1.21 (0.982 ... 1.38)	-0.19 (-0.38 ... -0.080)	38.55

HighResMIP-EC-Earth3P (1)	good	good	1.32 (1.08 ... 1.54)	-0.35 (-0.62 ... -0.18)	39.096
HighResMIP-HadGEM3-GC31-HM (1)	good	good	0.891 (0.737 ... 1.02)	-0.12 (-0.24 ... -0.0030)	39.787
HighResMIP-HadGEM3-GC31-LM (1)	good	good	0.962 (0.794 ... 1.10)	-0.12 (-0.32 ... 0.0050)	38.949
HighResMIP-HadGEM3-GC31-MM (1)	good	good	0.880 (0.651 ... 1.02)	-0.12 (-0.25 ... 0.040)	39.015
HighResMIP-MPI-ESM1-2-HR (1)	good	good	0.943 (0.751 ... 1.08)	-0.083 (-0.19 ... 0.068)	36.812
HighResMIP-MPI-ESM1-2-XR (1)	good	good	0.931 (0.715 ... 1.07)	-0.26 (-0.44 ... 0.0050)	35.405
UKCP18 land-GCM PPE (1) rcp85 ppe ()	good	good	1.05 (0.888 ... 1.18)	-0.29 (-0.45 ... -0.16)	
UKCP18 land-GCM PPE (2) rcp85 ppe ()	good	good	1.03 (0.822 ... 1.16)	-0.17 (-0.33 ... -0.023)	40.471
UKCP18 land-GCM PPE (3) rcp85 ppe ()	good	good	0.841 (0.683 ... 0.951)	-0.17 (-0.27 ... -0.052)	41.148
UKCP18 land-GCM PPE (4) rcp85 ppe ()	good	good	0.983 (0.776 ... 1.13)	-0.22 (-0.35 ... -0.067)	40.511
UKCP18 land-GCM PPE (5) rcp85 ppe ()	good	good	1.08 (0.823 ... 1.24)	-0.20 (-0.36 ... 0.043)	39.867
UKCP18 land-GCM PPE (6) rcp85 ppe ()	good	good	0.731 (0.603 ... 0.821)	-0.15 (-0.31 ... 0.019)	42.253
UKCP18 land-GCM PPE (7) rcp85 ppe ()	good	good	0.942 (0.749 ... 1.08)	-0.21 (-0.40 ... -0.10)	40.358
UKCP18 land-GCM PPE (8) rcp85 ppe ()	good	good	0.805 (0.639 ... 0.936)	-0.26 (-0.40 ... -0.14)	40.064
UKCP18 land-GCM PPE (9) rcp85 ppe ()	good	good	0.937 (0.709 ... 1.12)	-0.063 (-0.16 ... 0.10)	41.246
UKCP18 land-GCM PPE (10) rcp85 ppe ()	good	good	0.772 (0.641 ... 0.871)	-0.24 (-0.38 ... -0.10)	40.499
UKCP18 land-GCM PPE (11) rcp85 ppe ()	good	good	1.10 (0.824 ... 1.29)	-0.20 (-0.33 ... -0.024)	38.424
UKCP18 land-GCM PPE (12) rcp85 ppe ()	good	good	1.11 (0.941 ... 1.24)	-0.23 (-0.36 ... -0.12)	42.2
UKCP18 land-GCM PPE (13) rcp85 ppe ()	good	good	1.00 (0.748 ... 1.17)	-0.22 (-0.38 ... 0.013)	42.414
UKCP18 land-GCM PPE (14) rcp85 ppe ()	good	good	0.952 (0.759 ... 1.09)	-0.17 (-0.30 ... -0.035)	40.273
UKCP18 land-GCM PPE (15) rcp85 ppe ()	good	good	0.993 (0.751 ... 1.16)	-0.27 (-0.39 ... -0.074)	40.223
CMIP6-ACCESS-CM2_r1i1p1f1 ()	good	good	1.11 (0.850 ... 1.29)	-0.20 (-0.46 ... -0.090)	
CMIP6-ACCESS-ESM1-5_r1i1p1f1 ()	good	good	1.00 (0.780 ... 1.17)	-0.23 (-0.39 ... -0.090)	
CMIP6-CanESM5_r1i1p1f1 ()	good	good	0.940 (0.780 ... 1.10)	-0.21 (-0.40 ... -0.090)	
CMIP6-CMCC-ESM2_r1i1p1f1 ()	good	good	0.880 (0.660 ... 1.04)	-0.18 (-0.35 ... 0.050)	
CMIP6-CNRM-CM6-1-HR_r1i1p1f2 ()	good	good	0.850 (0.680 ... 1.00)	-0.13 (-0.31 ... 0.080)	
CMIP6-CNRM-CM6-1_r1i1p1f2 ()	good	good	1.17 (0.850 ... 1.38)	-0.30 (-0.48 ... -0.11)	
CMIP6-CNRM-ESM2-1_r1i1p1f2 ()	good	good	0.950 (0.810 ... 1.13)	-0.25 (-0.61 ... -0.13)	
CMIP6-EC-Earth3_r1i1p1f1 ()	good	good	1.17 (0.920 ... 1.39)	-0.41 (-0.74 ... -0.26)	
CMIP6-EC-Earth3-CC_r1i1p1f1 ()	good	good	1.12 (0.870 ... 1.33)	-0.28 (-0.56 ... -0.13)	
CMIP6-EC-Earth3-Veg_r1i1p1f1 ()	good	good	1.18 (0.930 ... 1.41)	-0.22 (-0.46 ... -0.020)	
CMIP6-EC-Earth3-Veg-LR_r1i1p1f1 ()	good	good	1.40 (1.14 ... 1.62)	-0.32 (-0.50 ... -0.16)	
CMIP6-FGOALS-g3_r1i1p1f1 ()	good	good	0.710 (0.560 ... 0.830)	-0.16 (-0.35 ... 0.080)	
CMIP6-GISS-E2-1-G_r1i1p1f2 ()	good	good	1.09 (0.870 ... 1.33)	-0.28 (-0.57 ... -0.070)	
CMIP6-HadGEM3-GC31-LL_r1i1p1f3 ()	good	good	1.22 (1.01 ... 1.47)	-0.31 (-0.75 ... -0.18)	
CMIP6-HadGEM3-GC31-MM_r1i1p1f3 ()	good	good	1.12 (0.930 ... 1.28)	-0.29 (-0.45 ... -0.14)	
CMIP6-INM-CM4-8_r1i1p1f1 ()	good	good	1.10 (0.830 ... 1.33)	-0.29 (-0.48 ... -0.060)	
CMIP6-INM-CM5-0_r1i1p1f1 ()	good	good	0.970 (0.800 ... 0.970)	-0.52 (-0.54 ... -0.42)	
CMIP6-IPSL-CM6A-LR_r1i1p1f1 ()	good	good	0.890 (0.700 ... 1.05)	-0.22 (-0.42 ... 0.040)	
CMIP6-KACE-1-0-G_r1i1p1f1 ()	bad	good	0.780 (0.620 ... 0.950)	-0.25 (-0.50 ... -0.060)	
CMIP6-MIROC6_r1i1p1f1 ()	bad	bad	1.37 (1.12 ... 1.60)	-0.24 (-0.62 ... -0.11)	
CMIP6-MPI-ESM1-2-HR_r1i1p1f1 ()	good	good	0.900 (0.690 ... 1.05)	-0.24 (-0.47 ... -0.10)	

CMIP6-MPI-ESM1-2-LR_r1i1p1f1 ()	good	good	1.02 (0.850 ... 1.17)	-0.40 (-0.66 ... -0.27)	
CMIP6-MRI-ESM2-0_r1i1p1f1 ()	good	good	1.11 (0.800 ... 1.29)	-0.16 (-0.28 ... 0.040)	
CMIP6-NESM3_r1i1p1f1 ()	bad	good	0.780 (0.590 ... 0.940)	-0.18 (-0.34 ... 0.060)	
CMIP6-NorESM2-LM_r1i1p1f1 ()	good	good	0.820 (0.670 ... 0.960)	-0.14 (-0.30 ... 0.030)	
CMIP6-NorESM2-MM_r1i1p1f1 ()	good	good	0.930 (0.740 ... 1.10)	-0.070 (-0.34 ... #REF!)	
CMIP6-TaiESM1_r1i1p1f1 ()	good	good	1.16 (0.940 ... 1.33)	-0.19 (-0.42 ... -0.060)	
CMIP6-UKESM1-0-LL_r1i1p1f2 ()	good	good	0.990 (0.790 ... 1.15)	-0.010 (-0.23 ... 0.15)	
CORDEX22-HADGEMr1-REMO ()	good	good	0.680 (0.510 ... 0.870)	-0.28 (-0.83 ... 0.0)	
CORDEX22-HADGEMr1-REGCM ()	good	good	0.770 (0.590 ... 0.910)	-0.15 (-0.33 ... 0.010)	
CORDEX22-MPIr1-REMO ()	good	good	1.03 (0.760 ... 1.31)	-0.21 (-0.57 ... 0.080)	
CORDEX22-MPIr1-REGCM ()	good	good	0.820 (0.600 ... 1.01)	-0.19 (-0.65 ... 0.040)	
CORDEX22-NORESMr1-REMO ()	good	good	0.610 (0.470 ... 0.780)	-0.23 (-0.58 ... 0.0)	
CORDEX22-NORESMr1-REGCM ()	good	good	0.710 (0.560 ... 0.880)	-0.35 (-0.70 ... -0.14)	

5 Multi-method multi-model attribution

This section shows Probability Ratios and change in rain event intensity ΔI for models. Table 3 shows the model-based results for the models that are labeled 'reasonable' or 'good'.

Table 3. Probability ratio and change in intensity for models that passed the validation tests for (a) past vs. present and (b) present vs. future.

	a. Past vs. present		**b. Present vs. future**	
Observations/Model	**Probability ratio PR [-]**	**Change in intensity ΔI [°C]**	**Probability ratio PR [-]**	**Change in intensity ΔI [°C]**
ERA5	27 (5.7 ... ∞)	2.2 (1.3 ... 3.0)		
CPC	2.8e+2 (13 ... ∞)	3.7 (2.2 ... 5.3)		
	(...)	(...)		
CORDEX44-CNRMr1-RCA ()	13 (2.2 ... 1.0e+4)	0.87 (0.19 ... 1.6)	5.6 (0.00010 ... 31)	0.80 (0.30 ... 1.4)
CORDEX44-MK3r1-RCA ()	13 (2.1 ... 1.0e+4)	1.3 (0.36 ... 2.4)	5.5 (0.78 ... 41)	1.3 (0.41 ... 2.1)
CORDEX44-IPSLr1-RCA ()	4.0e+6 (19 ... 1.0e+4)	1.8 (1.1 ... 2.6)	7.0 (2.6 ... 98)	1.3 (0.81 ... 1.7)
CORDEX44-CORDEX44-MIROCr1-RCA ()	4.0 (0.95 ... 1.0e+4)	0.62 (-0.050 ... 1.3)	6.4 (0.00010 ... 36)	1.3 (0.45 ... 2.1)
CORDEX44-HADGEMr1-RCA ()	55 (2.2 ... 1.0e+4)	0.79 (-0.010 ... 1.4)	8.0 (3.1 ... 24)	1.3 (0.88 ... 1.7)
CORDEX44-MPIr1-REMO ()	23 (2.9 ... 1.0e+4)	1.6 (0.89 ... 2.2)	2.8 (1.1 ... 8.4)	0.72 (0.060 ... 1.3)
CORDEX44-MPIr1-RCA ()	19 (4.0 ... 1.0e+4)	1.6 (1.1 ... 2.1)	6.8 (3.2 ... 24)	1.3 (0.85 ... 1.8)
CORDEX44-NORESMr1-RCA ()	10 (1.3 ... 1.0e+4)	1.0 (0.17 ... 2.2)	5.0 (1.2 ... 36)	1.2 (0.49 ... 1.9)
CORDEX44-GFDLr1-REGCM ()	2.6 (0.060 ... 1.0e+4)	0.39 (-1.0 ... 1.7)	2.1 (0.58 ... 13)	0.47 (-0.18 ... 1.1)
CORDEX44-GFDLr1-RCA ()	1.0e+4 (6.9 ... 1.0e+4)	1.2 (0.46 ... 2.0)	4.5 (0.00010 ... 2.2e+2)	0.99 (0.36 ... 1.6)
HighResMIP-HadGEM3-GC31-HM (1)	28 (5.3 ... ∞)	1.8 (1.0 ... 2.6)	(...)	(...)
HighResMIP-HadGEM3-GC31-LM (1)	4.1 (1.2 ... ∞)	0.90 (0.13 ... 1.9)	(...)	(...)
HighResMIP-HadGEM3-GC31-MM (1)	99 (7.7 ... ∞)	2.1 (1.3 ... 3.0)	(...)	(...)

HighResMIP-MPI-ESM1-2-HR (1)	7.1 (1.8 ... 95)	1.3 (0.48 ... 2.2)	(...)	(...)
HighResMIP-MPI-ESM1-2-XR (1)	3.1 (0.38 ... ∞)	0.43 (-0.55 ... 1.2)	(...)	(...)
UKCP18 land-GCM PPE (1) rcp85 ppe ()	5.3e+4 (16 ... 1.0e+6)	1.4 (0.57 ... 2.1)	5.9 (3.6 ... 50)	0.84 (0.65 ... 1.0)
UKCP18 land-GCM PPE (4) rcp85 ppe ()	1.6e+2 (8.1 ... 1.0e+6)	1.6 (1.0 ... 2.2)	3.8 (2.9 ... 5.8)	1.1 (0.89 ... 1.3)
UKCP18 land-GCM PPE (5) rcp85 ppe ()	47 (3.4 ... 1.0e+6)	1.6 (0.89 ... 2.4)	3.8 (2.3 ... 8.1)	0.83 (0.65 ... 1.0)
UKCP18 land-GCM PPE (6) rcp85 ppe ()	8.2e+2 (13 ... 1.0e+6)	2.0 (1.5 ... 2.5)	9.0 (4.7 ... 36)	1.0 (0.91 ... 1.2)
UKCP18 land-GCM PPE (7) rcp85 ppe ()	7.9e+2 (24 ... 1.0e+6)	1.9 (1.3 ... 2.5)	5.6 (3.7 ... 32)	1.2 (1.0 ... 1.5)
UKCP18 land-GCM PPE (9) rcp85 ppe ()	9.2 (3.4 ... 2.0e+2)	1.6 (1.1 ... 2.1)	3.6 (2.5 ... 6.6)	1.0 (0.85 ... 1.2)
UKCP18 land-GCM PPE (10) rcp85 ppe ()	7.7e+4 (9.1 ... 1.0e+6)	1.4 (0.83 ... 2.1)	5.6 (4.1 ... 8.7)	1.1 (0.89 ... 1.2)
UKCP18 land-GCM PPE (11) rcp85 ppe ()	3.4e+2 (7.3 ... 1.0e+6)	2.1 (1.4 ... 2.9)	5.9 (3.5 ... 17)	1.1 (0.98 ... 1.3)
UKCP18 land-GCM PPE (12) rcp85 ppe ()	3.2e+2 (9.5 ... 1.0e+6)	1.8 (0.90 ... 2.7)	5.3 (3.5 ... 21)	0.97 (0.75 ... 1.2)
UKCP18 land-GCM PPE (13) rcp85 ppe ()	8.6 (2.3 ... 1.0e+6)	0.91 (0.22 ... 1.5)	3.0 (2.3 ... 4.6)	0.74 (0.57 ... 0.91)
UKCP18 land-GCM PPE (15) rcp85 ppe ()	2.3e+3 (4.3 ... 1.0e+6)	1.4 (0.76 ... 2.0)	5.5 (3.7 ... 11)	0.95 (0.80 ... 1.1)
CMIP6-ACCESS-CM2_r1i1p1f1 ()	2.6 (0.44 ... 1.0e+4)	0.54 (-0.40 ... 1.4)	7.1 (0.00010 ... 28)	1.1 (0.76 ... 1.6)
CMIP6-ACCESS-ESM1-5_r1i1p1f1 ()	16 (3.0 ... 1.0e+4)	1.0 (0.37 ... 1.7)	7.5 (0.00010 ... 1.2e+2)	0.95 (0.61 ... 1.4)
CMIP6-CanESM5_r1i1p1f1 ()	2.2e+2 (13 ... 1.0e+4)	1.7 (1.1 ... 2.2)	4.9 (0.00010 ... 1.1e+2)	1.1 (0.82 ... 1.3)
CMIP6-CMCC-ESM2_r1i1p1f1 ()	3.7 (0.82 ... 1.0e+4)	0.61 (-0.12 ... 1.4)	6.5 (0.00010 ... 55)	1.3 (0.59 ... 2.0)
CMIP6-CNRM-CM6-1-HR_r1i1p1f2 ()	37 (3.5 ... 1.0e+4)	1.7 (0.86 ... 2.6)	4.9 (2.6 ... 19)	1.0 (0.66 ... 1.3)
CMIP6-CNRM-CM6-1_r1i1p1f2 ()	2.7 (0.29 ... 1.0e+4)	0.41 (-0.45 ... 1.3)	2.7 (1.2 ... 11)	0.74 (0.26 ... 1.2)
CMIP6-CNRM-ESM2-1_r1i1p1f2 ()	5.9 (1.1 ... 1.0e+4)	0.65 (-0.020 ... 1.3)	6.8 (0.00010 ... 41)	1.4 (0.85 ... 2.2)
CMIP6-EC-Earth3-CC_r1i1p1f1 ()	85 (4.5 ... 1.0e+4)	1.3 (0.59 ... 2.5)	2.5 (0.39 ... 14)	0.74 (-0.59 ... 1.9)
CMIP6-EC-Earth3-Veg_r1i1p1f1 ()	10 (2.6 ... 1.0e+4)	1.1 (0.47 ... 1.8)	2.0 (0.00010 ... 14)	0.42 (-0.20 ... 0.99)
CMIP6-GISS-E2-1-G_r1i1p1f2 ()	2.9 (0.12 ... 1.0e+4)	0.43 (-1.1 ... 2.3)	3.2 (1.4 ... 21)	0.59 (0.18 ... 1.0)
CMIP6-HadGEM3-GC31-LL_r1i1p1f3 ()	1.0e+4 (15 ... 1.0e+4)	1.7 (0.92 ... 2.4)	4.5 (2.1 ... 23)	1.0 (0.59 ... 1.5)
CMIP6-HadGEM3-GC31-MM_r1i1p1f3 ()	1.0e+4 (11 ... 1.0e+4)	1.9 (1.0 ... 2.8)	3.3 (2.1 ... 6.9)	1.1 (0.52 ... 1.4)
CMIP6-INM-CM4-8_r1i1p1f1 ()	1.0e+4 (3.2 ... 1.0e+4)	1.7 (0.31 ... 2.8)	7.9 (3.3 ... 28)	1.6 (0.78 ... 2.1)
CMIP6-IPSL-CM6A-LR_r1i1p1f1 ()	13 (2.3 ... 1.0e+4)	0.90 (0.14 ... 1.8)	11 (0.00010 ... 2.5e+2)	1.5 (0.42 ... 1.9)
CMIP6-MPI-ESM1-2-HR_r1i1p1f1 ()	1.7e+2 (6.0 ... 1.0e+4)	1.3 (0.39 ... 2.1)	3.3 (2.0 ... 10)	0.96 (0.56 ... 1.4)
CMIP6-MRI-ESM2-0_r1i1p1f1 ()	3.6 (0.94 ... 58)	0.81 (-0.040 ... 1.6)	2.8 (0.00010 ... 6.1)	0.71 (0.13 ... 1.4)
CMIP6-NorESM2-LM_r1i1p1f1 ()	14 (2.2 ... 1.0e+4)	1.2 (0.46 ... 2.0)	3.7 (0.65 ... 16)	0.62 (0.020 ... 1.2)
CMIP6-NorESM2-MM_r1i1p1f1 ()	2.4 (0.45 ... 5.0e+3)	0.66 (-0.34 ... 1.6)	4.1 (0.00010 ... 36)	0.60 (0.030 ... 1.1)
CMIP6-TaiESM1_r1i1p1f1 ()	6.0 (1.5 ... 1.0e+4)	1.0 (0.18 ... 1.8)	6.4 (3.2 ... 29)	1.1 (0.84 ... 1.5)
CMIP6-UKESM1-0-LL_r1i1p1f2 ()	3.8 (2.1 ... 1.0e+3)	1.3 (0.77 ... 1.8)	2.8 (1.7 ... 11)	0.82 (0.52 ... 1.2)
CORDEX22-MPIr1-REMO ()	3.1 (0.35 ... 1.0e+4)	0.57 (-0.57 ... 1.6)	3.0 (1.5 ... 19)	0.82 (0.37 ... 1.3)
CORDEX22-MPIr1-REGCM ()	11 (1.5 ... 1.0e+4)	0.90 (0.0 ... 1.8)	9.1 (0.00010 ... 7.4e+2)	1.3 (0.97 ... 1.7)

6 Hazard synthesis

For the event definitions described above we evaluate the influence of anthropogenic climate change on the events by calculating the probability ratio as well as the change in intensity using observations and climate models. Models which do not pass (marked in red in table 2) the validation tests described above are excluded from the analysis. The aim is to synthesise results from models that pass the evaluation along with the observations-based products, to give an overarching attribution statement. Figs. 5-6 show the changes in probability and intensity for the observation-based products (blue) and models (red). To combine them into a synthesised assessment, a term to account for intermodel spread is added (in quadrature) to the natural variability of the models. This is shown in the figures as white boxes around the light red bars (in this study, only the intensity changes show intermodel spread beyond the models' natural variability). The dark red bar shows the model average, consisting of a weighted mean using the (uncorrelated) uncertainties due to natural variability plus the term representing intermodel spread (i.e., the inverse square of the white bars). Observation-based products and models are combined into a single result in two ways. Firstly, we neglect common model uncertainties beyond the intermodel spread that is depicted by the model average, and compute the weighted average of models (dark red bar) and observations (blue bar): this is indicated by the magenta bar. As, due to common model uncertainties, model uncertainty can be larger than the intermodel spread, secondly, we also show the more conservative estimate of an unweighted, direct average of observations (dark red bar) and models (dark blue bar) contributing 50% each, indicated by the white box around the magenta bar in the synthesis figures.

For the probability ratio, the best estimate of the models combined is well within the uncertainty of the observed change and the weighted synthesised probability ratio is 60 (35-120). Given however, that the discrepancy between individual models wrt best guess is very large, spanning orders of magnitude and the quantification of changes in heat extremes is notoriously difficult, we report the best guess of a PR of 60 as our main result, but use the unweighted uncertainty to estimate the lower and upper bound: 9-1300. For the change in intensity we notice that the observed increase in intensity is larger than that of the models but again well within the uncertainty bounds. For the same reasons as above we also report the unweighted bounds as our overarching result. The change in intensity attributable to human-induced climate change is 1.4 (0.8-3.4).

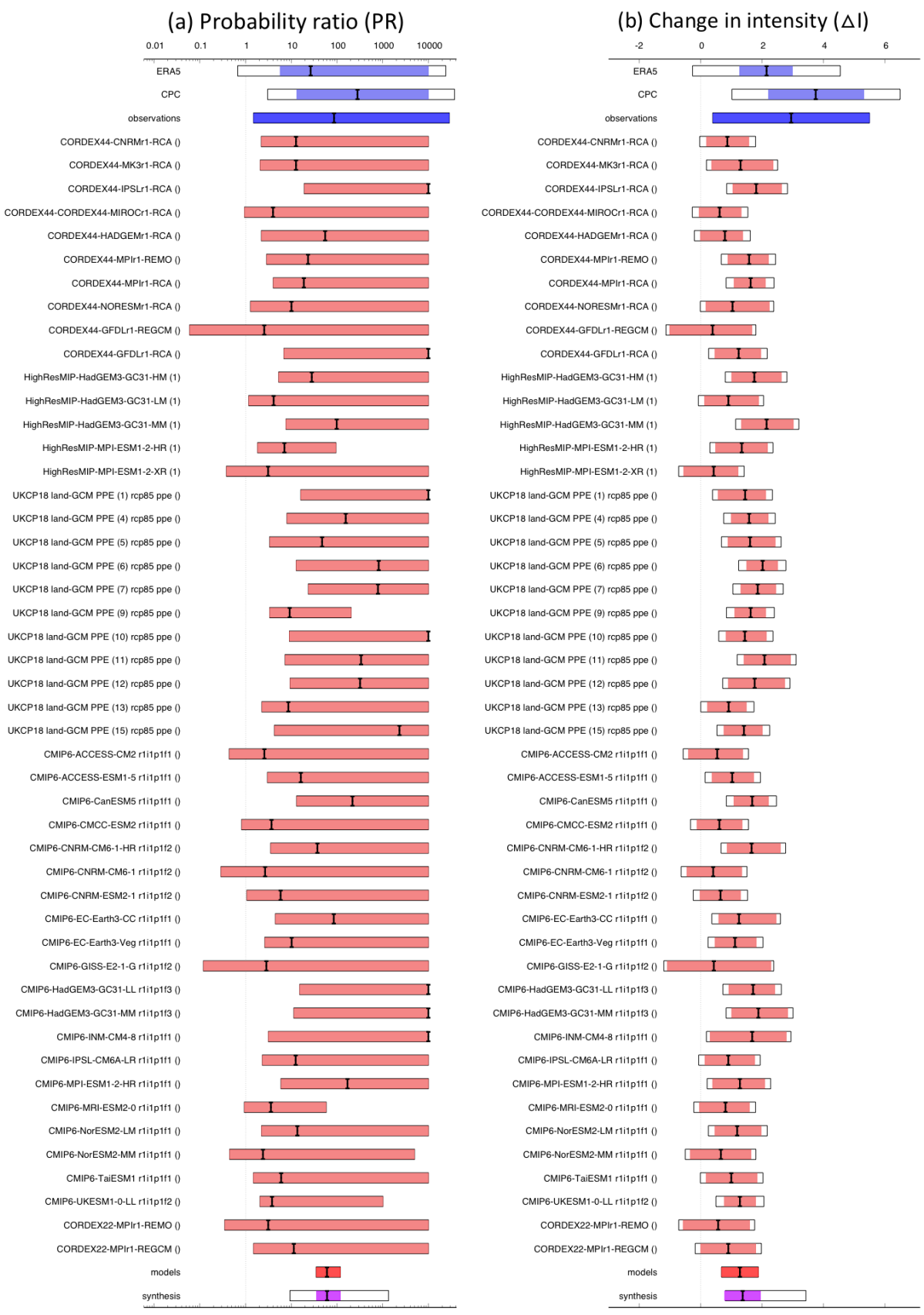
(a) Probability ratio (PR)
0.01
0.1
1
10
100
1000
10000
(b) Change in intensity (ΔI)
-2
0
2
4
6
ERA5
CPC
observations
CORDEX44-CNRMr1-RCA ()
CORDEX44-MK3r1-RCA ()
CORDEX44-IPSLr1-RCA ()
CORDEX44-CORDEX44-MIROCr1-RCA ()
CORDEX44-HADGEMr1-RCA ()
CORDEX44-MPIr1-REMO ()
CORDEX44-MPIr1-RCA ()
CORDEX44-NORESMr1-RCA ()
CORDEX44-GFDLr1-REGCM ()
CORDEX44-GFDLr1-RCA ()
HighResMIP-HadGEM3-GC31-HM (1)
HighResMIP-HadGEM3-GC31-LM (1)
HighResMIP-HadGEM3-GC31-MM (1)
HighResMIP-MPI-ESM1-2-HR (1)
HighResMIP-MPI-ESM1-2-XR (1)
UKCP18 land-GCM PPE (1) rcp85 ppe ()
UKCP18 land-GCM PPE (4) rcp85 ppe ()
UKCP18 land-GCM PPE (5) rcp85 ppe ()
UKCP18 land-GCM PPE (6) rcp85 ppe ()
UKCP18 land-GCM PPE (7) rcp85 ppe ()
UKCP18 land-GCM PPE (9) rcp85 ppe ()
UKCP18 land-GCM PPE (10) rcp85 ppe ()
UKCP18 land-GCM PPE (11) rcp85 ppe ()
UKCP18 land-GCM PPE (12) rcp85 ppe ()
UKCP18 land-GCM PPE (13) rcp85 ppe ()
UKCP18 land-GCM PPE (15) rcp85 ppe ()
CMIP6-ACCESS-CM2 r1i1p1f1 ()
CMIP6-ACCESS-ESM1-5 r1i1p1f1 ()
CMIP6-CanESM5 r1i1p1f1 ()
CMIP6-CMCC-ESM2 r1i1p1f1 ()
CMIP6-CNRM-CM6-1-HR r1i1p1f2 ()
CMIP6-CNRM-CM6-1 r1i1p1f2 ()
CMIP6-CNRM-ESM2-1 r1i1p1f2 ()
CMIP6-EC-Earth3-CC r1i1p1f1 ()
CMIP6-EC-Earth3-Veg r1i1p1f1 ()
CMIP6-GISS-E2-1-G r1i1p1f2 ()
CMIP6-HadGEM3-GC31-LL r1i1p1f3 ()
CMIP6-HadGEM3-GC31-MM r1i1p1f3 ()
CMIP6-INM-CM4-8 r1i1p1f1 ()
CMIP6-IPSL-CM6A-LR r1i1p1f1 ()
CMIP6-MPI-ESM1-2-HR r1i1p1f1 ()
CMIP6-MRI-ESM2-0 r1i1p1f1 ()
CMIP6-NorESM2-LM r1i1p1f1 ()
CMIP6-NorESM2-MM r1i1p1f1 ()
CMIP6-TaiESM1 r1i1p1f1 ()
CMIP6-UKESM1-0-LL r1i1p1f2 ()
CORDEX22-MPIr1-REMO ()
CORDEX22-MPIr1-REGCM ()
models
synthesis

Figure 5: Synthesis of (a) probability ratios and (b) intensity changes when comparing the return period and magnitudes of the 7-day average maximum temperatures over the study region in the current climate and a 1.2°C cooler climate.

Looking at the simulations of potential further changes in a 0.8℃ warmer world compared with today we find that while some models have a lower bound below unity for the probability ratio all best estimates are greater than 1 and show, as expected in a warming world, a further increase of a factor of 4 in the likelihood of a heatwave like the observed to occur. This is an order of magnitude smaller than the thus far observed change in likelihood of a factor of approx. 60 which cannot be explained by the slightly smaller GMST change alone. Thus, without further analysis as to why these changes are so different, we do treat the quantitative estimate with caution. The change in intensity with a further 0.8℃ of warming is 1 (0.8-1.2) which is very much in line with the estimated changes in intensity that have occurred up to present and highlights again that, for heat waves, changes in intensity are much less sensitive to individual models and methods and thus the more reliable quantitative results to communicate.

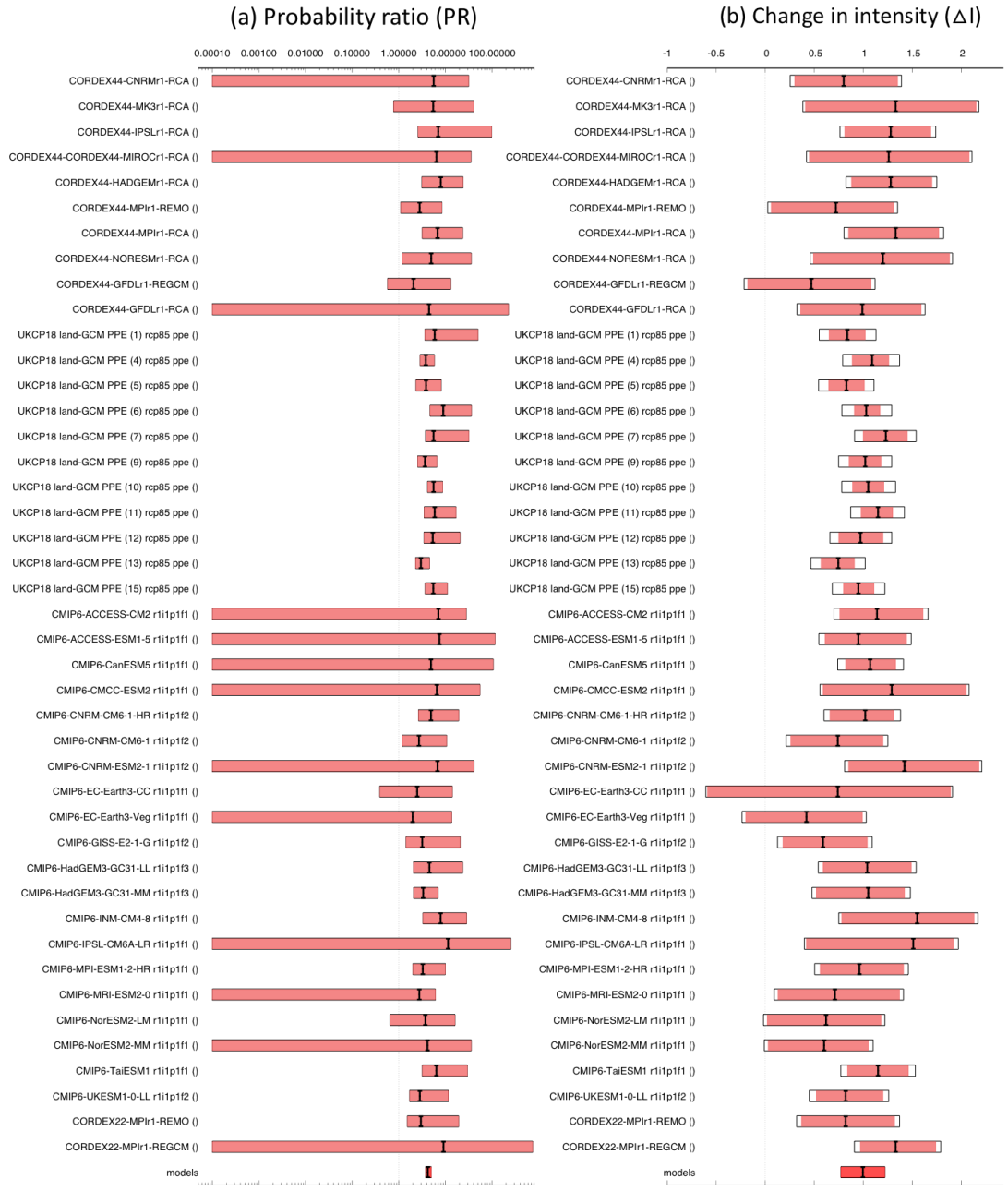

Figure 6: As Fig. 5, but for models only of a 0.8°C warmer (2°C since pre-industrial) climate.

7 Vulnerability and exposure

Heatwaves are amongst the deadliest natural hazards with thousands of people dying from heat-related causes each year (IFRC, 2020). However, the full impact of a heatwave is often not known until weeks or months afterwards, once death certificates are collected, and data on excess deaths is analysed. Impacts are an effect of pre-existing social, economic, political conditions which leads to people's vulnerabilities. Data on excess deaths was not available at the time of writing, however it is notable that this heatwave occurred very early in the austral summer season, likely before people were acclimated to higher temperatures. Early season heatwaves are known to be more deadly because people may not be prepared (e.g. haven't taken out fans or other cooling devices) or acclimatized to high temperatures (Diaz et al., 2002; Anderson et al., 2011).

7.1 Vulnerable Groups

A study of 326 Latin American cities found that marginal increases in hot temperatures results in a steep increase in mortality, and that those with respiratory infections and diseases, and those over the age of 65 tended to result in a higher fraction of excess deaths (Kephart et al., 2022). At the individual level, people with pre-existing health conditions, those that are over 65 or under five, have low incomes, work indoors with poor ventilation in homes or factories, and outdoor workers are more vulnerable to heat stress, heat stroke, or death (Stafoggia et al., 2006; Green et al., 2019). There are also societal components of vulnerability including adaptive capacity and population density that can increase the impacts of extreme heat.

However, heatwaves do not need to result in excess deaths. Simple actions like checking in on your neighbors, drinking enough water, and finding a cool place to go during the hottest part of the day can reduce impacts (Singh et al., 2019).

7.2 Heatwave Early Warning Systems

While Paraguay has yet to develop a heatwave early warning system (Climate Knowledge Portal, 2021), Argentina established one in 2018 which provides early warnings with recommended actions to the general population and at-risk groups (Servicio Meteorológico Nacional Argentina, 2018). If there is a heat risk alert (yellow, orange, or red) for the following 24 hours, the Ministry of Security and the Ministry of Health are notified and the Ministry of Health will launch an epidemiological alert and make it public through social media, press agencies, and national media. For central and northern Argentina, the first heat warning was issued on December 2, two days prior to the start of the December heatwave (SMN, 2022). In the case of Paraguay, a special bulletin for persistent high temperatures was issued during December 7, while the same day Uruguayan authorities released a heatwave warning for the western portion of the country.

Governments, city authorities and civil society organizations can prevent heat-related impacts by acting in anticipation of a forecast heatwave, after the issuance of an early warning and before the heatwave onset. Such early actions can include setting up temporary cooling centres in public spaces,

and reinforcing health care services with extra staff, which is done in cities such as Hanoi, Vietnam and Ahmedabad, India (Anticipation Hub, n.d.; NRDC, 2019).

7.3 Informality and urban planning for heat

Cities are often hotspots of heat risk due to the urban heat island effect, and the fact that socio-economically disadvantaged populations tend to live in hotter parts of the city, often in informal settlements (IPCC AR6). Research shows that built-up urban areas, where most low-income residents live, can become significantly hotter than its rural surroundings and with expanding urban land this effect will intensify in the future (Huang et al., 2019). Worth noting is that Argentina is amongst the most urbanized countries in the world, with 92 percent of people living in urban areas (Bolay, 2019).

In contrast, Paraguay is only about 62 percent urban (STATISTA, 2022), but, over half of the country's poor population resides in urban areas, where inadequate implementation of land use and public planning aggravate urban inequality and render people more exposed to threats such as extreme heat (Casseb, Cantero and Gossen, 2022a). In the Metropolitan Area of Asunción, over 400 informal settlements are home to 38.000 residents. Less than one percent of these inhabitants have access to sanitary sewages and 12 percent lack piped water, increasing their risk of contracting disease and reducing their coping capacity to extreme heat (Casseb, Cantero and Gossen, 2022b; Sandoval and Samiento, 2020).

Launched in 2016 and 2018, respectively, Paraguay's *National Climate Change Adaptation Plan* and *National Climate Change Policy* provide the country's framework for adaptation and mitigation (Climate Knowledge Portal, 2021). The documents outline planned measures, including investments in research and training programmes on climate-related disease, local capacity-strengthening training on communication for health prevention, development of a communication strategy for disaster risk reduction and climate change adaptation, and mainstreaming of climate change in the curriculum of the educational system (SEAM/PNUD/FMAM, 2017). Implementation of these policies and heat-specific actions plans at scale could reduce the impacts of future heatwaves.

In Argentina, approximately 1 in 6 people live in informal settlements, with the majority of informal settlements located in the city of Buenos Aires totaling roughly 300,000 people (Vera and Sordi, 2021; C40, 2019). Critically, nearly 70 percent of homes located in informal neighborhoods do not have access to formal electricity, an essential requirement to face high temperatures (Vera and Sordi, 2021). Social cohesion can reduce heat-related mortality, but in informal settlements in Argentina, a lack of public spaces and recreational areas limits social cohesion and development (Yardley et al., 2011; Browning et al., 2006; Vera and Sordi, 2021).

In order to address the challenges associated with climate change, Buenos Aires adopted its first *Climate Adaptation and Mitigation Act* in 2011, launched the city's *Second Climate Action Plan* in 2015, and in 2020, introduced the ambitious *Climate Action Plan for 2050* (Government of the City of Buenos, 2020). In 2016, Buenos Aires launched its *Adaptation Program for Extreme Weather Conditions*, followed by the *Citizens ready against climate change* program in 2017, which has enabled over 2,700 people to attend workshops on heat risk with eight leaders from vulnerable communities to be trained to replicate them (c40, 2020; Massy and Gómez, 2020). By 2019, the city created 110 hectares of new green areas and a 290-hectare sized ecological natural reserve (Government of the City of Buenos, 2020). The 2019 *Vegetation Cover of Buenos Aires* report, provided detailed data on urban heat island risk, including the relationship between absorbing

surfaces, green spaces, and population density and could be used to plan for increased greening (Government of the City of Buenos, 2020, p. 63). The *Climate Action Plan for 2050*, outlines additional measures to be rolled out to reduce heat risk, notably including an increase of urban trees and the city's urban afforestation work by over 20 percent, implementing new pedestrian areas throughout densely populated city neighborhoods, creating green streets to act as biodiversity corridors and heat sinks to connect large green spaces, and expanding on the *Adaptation to Extreme Climate Events Program* which helps elderly residents to prepare for and cope with heatwaves (Government of the City of Buenos, 2020).

Publicly acclaimed for its urban sustainability project *Sustainable Food Production for a Resilient Rosario*, which was launched in 2001 following the Argentine economic collapse, the city of Rosario converts unoccupied land for food production while providing jobs and social benefits as well as increasing resilience to extreme heat (IIED, 2021; WRI, 2021). Another city in the heatwave prone northern part of Argentina, Mendoza, has developed the *Climate Change Laboratory of the City of Mendoza* as a platform to develop sustainable local public policy to the glocal issue through design, innovation, and experimentation (Open Government Partnership, 2021). These are positive steps towards limiting resident's exposure and vulnerability to extreme heat, and require further expansion to additional cities.

7.4 Indoor Heat

On the household level, ensuring the availability of electricity to power cooling devices is critical. Active cooling, such as deploying air conditioners and fans, are common means of controlling indoor temperatures to stay within levels of thermal comfort (see e.g. Lee and Shaman, 2017; Zander et al., 2021). Maintaining indoor thermal comfort, reducing the impacts from extreme heat on people, can also be achieved through passive cooling by making heat-informed design choices of buildings, including the implementation of green or cool roof and wall technologies (Saffari et al., 2018). Passive cooling helps avoid the risk of overtaxing the electricity grid and exacerbating greenhouse gas emissions while reducing energy bills, making such measures more sustainable (Synnefa and Santamouris, 2012; Seifhashemi et al., 2018; Dabaieh et al., 2015). Importantly, implementing cool and green roofs can also reduce the overall urban heat island effect (Roman et al., 2016; Yang et al., 2018). As opposed to active cooling measures, heat-informed design helps mitigate the lethal risks associated with power cuts during heatwaves (Farbotko and Waitt, 2011; Filho et al., 2018), which were prevalent during the studied heat spell in Buenos Aires, Resistencia, Asunción, Alto Paraguay, and other cities, affecting hundreds of thousands of people across the two countries (Diario Conurbano, 2022; Página12, 2022; Memo, 2022; Diario Norte, 2022; La Nación, 2022; Ultima Hora, 2022).

In 2019, Buenos Aires adopted a new building code with consideration to managing extreme heat. Natural ventilation, envelope thermal insulation, green walls and roof, and solar gain and protection make out key guidelines in the new standard (Government of the City of Buenos, 2020). The Code determines that all new roofs and terraces must implement cool roof technology or allocate one-fourth of its surface to a green roof (C40, 2021). When implemented in schools, the latter has been known to provide an extra outdoor classroom for accessible learning about ecology and agriculture (Holcim Foundation, 2012). While there are examples of heat-informed urban planning and adaptation outside of the capital (Fabían et al., 2021), there would be notable benefits to their mainstreaming in other urban centers in heatwave-prone northern Argentina, some of which are up to twice as densely populated as Buenos Aires (such as La Plata) and home to a significant number of low-income

populations (such as Rosario, Córdoba, Tucumán, and Corrientes) (Vera and Sordi, 2021). In contrast, Paraguay does not currently have an energy building code nor widespread use of other heat-related interventions, negatively affecting the population's coping capacity during heatwaves (Silvero et al., 2019; Climate Knowledge Portal, 2021).

7.6 V&E Conclusion

Heatwaves are a regular occurrence in Paraguay and Argentina and as the attribution analysis indicates, these types of events are increasing in frequency and intensity, which adds urgency to the need to adapt to this new normal. Investments in improving heat early warning systems, urban planning for heat, and behavioural change communication can help to reduce heat impacts now and in the future.

Data availability

Almost all data will be available via the Climate Explorer.

References

All references are given as hyperlinks in the text.